Two-Dimensional Membranes with Highly Charged Nanochannels for Osmotic Energy Conversion

Yijun Qian,[a] Dan Liu,*[a] Guoliang Yang,[a] Jinqiu Chen,[a] Yuxi Ma,[a] Lifeng Wang,[a] Xungai Wang,[a] and Weiwei Lei*[a]

Inadequate mass transportation of semipermeable membranes causes poor osmotic energy conversion from salinity-gradient. Here, the lamellar graphene oxide membranes (GOMs) constructed with numerous fusiform-like nanochannels, that are pre-filled with negatively charged polyanion electrolytes, to both enhance the ion permeability and ion selectivity of the membrane for energy harvest from the salinty gradient, were developed. The as-prepared membrane achieved the maximum output power density of ~4.94 W m⁻² under a 50 fold salinity gradient, which is 3.5 fold higher than that of pristine GOM. The enhancement could be ascribed to the synergistic impact of the expanded nanochannels and the enhanced space charge density. Via feeding with the artificial salinity water and monovalent cation electrolytes, the system could realise the power output up to 14.7 W m⁻² and 34.1 W m⁻², respectively. Overall, this material design strategy could provide an alternative concept to effectively enhance ion transport of other two-dimensional (2D) membranes for specific purposes.

Introduction

With continuing economic development, increasing global energy demand and imminent climate change, the importance of obtaining a sustainable energy future for humanity without destroying our environment at the same time cannot be overstated.[1] As a prospective technology for harvesting electricity from the salinity gradient, harvesting osmotic power has successfully aroused the attention of researchers for decades due to its advantages of easy accessibility, eco-friendliness and huge reserves.[2] Although both pressure-retarded osmosis (PRO) and reverse electrodialysis (RED) can achieve the harvesting of osmotic energy, the latter seems more attractive to us as its much higher power density is predicted by modelling data and direct electricity capture from the system without using any external stimulus (e.g. turbine).[3] In fact, severely limited with the undeveloped technology in the past few decades, much focus has been only fixed on the optimization engineering of the ion exchange membrane (IEM) since the first IEM was applied to osmotic energy harvest between seawater and river water in 1954.[4] The recent advances in nanotechnology and material fabrication promote the development of the osmotic power generation under the

nanoscale phenomenon, especially for an unprecedented power density of 10^6 W m⁻² obtained from the nano-porous MoS₂, whilst the restricted high-tech, unaffordable expenditure and lab-scale fabrication still hinder the practical application.[5]

In recent years, nanomaterial membranes with charged nanopore structures ranging from metal organic frameworks (MOFs),[6] covalent organic frameworks (COFs),[7] carbon nanomaterials[8] and two-dimensional (2D) nanomaterials[9] are showing great promise to extract energy from the salinity gradient. 2D nanomaterial membranes, formed by stacking of neighbouring 2D nanosheets, have provided a promising and scalable alternative to harvest osmotic energy from the salinity gradient as their inside nanochannels are close to the Debye length and the intrinsic functionalities can induce charge-selective diffusion current.[10] However, the perfect ion-selective property within the sub-nanometer scale nanochannels inside the 2D membranes is usually realized by losing fast ion transport and restricting high ion flux, which results in a low power density far below the critical commercialized benchmark. To tackle this problem, the rational construction design of nanochannels that chooses sacrificial inorganic nanomaterials such as copper hydroxide nanowires or colloidal nanoparticles as intercalation of 2D membranes has been proposed.[11] After removing the intercalation, the membranes do display ultrahigh permeance when compared to the pristine ones, whilst the corresponding selectivity compromises brought by the expansion of the nanochannels. Similarly, for osmotic energy conversion, the potential drop in power output will occur accompanied by the overexpansion of the confined nanochannels, because the height of the nanochannels cannot overlap the Debye length, contributing to the loss of the cation selectivity. Thus, a high level of osmotic energy conversion of the 2D membranes requires the trade-off relationship between ion selectivity and ion transport flux.[12] In other words, the extra space charge needs to be provided to achieve efficient ion

[a] Y. Qian, Dr. D. Liu, G. Yang, J. Chen, Y. Ma, Dr. L. Wang, Prof. X. Wang, Prof. W. Lei
Institute for Frontier Materials
Deakin University
Locked Bag 20000, Geelong, Victoria 3220 (Australia)
E-mail: dan.liu@deakin.edu.au
weiwei.lei@deakin.edu.au

ChemSusChem

Research Article
doi.org/10.1002/cssc.202200933

Chemistry
Europe
European Chemical
Societies Publishing

selectivity when the nanochannels undergo expansion, which has been reported by previous studies.[13]

Polyelectrolytes with plenty of covalently linked ionized groups become charged in the polar solvent (e.g. water) and different interactions take place between charged functionalities and ions under the diverse nanoscales.[14] For example, MXene membranes can be endowed with unique lithium-ion sieving property by the introduction of poly(sodium 4-styrenesulfonate) (PSS) to their laminated membrane structure, where the compressed nanochannels within the sub-nanometre scale guarantee the direct interaction between dehydrated cations and sulfonated groups ($-SO_3$).[15] Besides, the hydrogel with the three-dimensional network structure can be negatively charged by adding PSS polyelectrolytes as space charge suppliers, which has the capability of accelerating the ion diffusion and facilitating the charge separation process when fixed under the nanometre scale confinement, showing the improvement of osmotic energy conversion.[16] However, studies on the combination of polyanion electrolytes and 2D membranes for osmotic energy harvest have been rarely reported.

Here, we propose the development of lamellar GOM with numerous fusiform-like channels with the heights of 2–8 nm, which are pre-filled with the polyanion electrolytes as the nanofluidic platform to harvest the salinity-gradient energy. The as-prepared membrane can simultaneously maintain a high cation selectivity and fast ion transport, which realizes a high power density output of ~4.94 W m^{-2} by mixing artificial seawater and artificial river water as the feeding sources. The osmotic energy conversion performance can be further improved to over 14.7 W m^{-2} by feeding high salinity water. In addition, compared with other monovalent electrolytes, an ultrahigh power output of 34.1 W m^{-2} from hydrogen chloride electrolytes can be ascribed to the effect of the high value of cation diffusion coefficient of H$^+$ with the small hydrated radius, which reveals the potential possibility of extracting salinity-gradient energy from the acid wastewater.

Results and Discussion

The fabrication of M-1 and M-2 is shown in Figure 1a. First, the Fe(OH)$_3$ colloidal solution (Tyndall effect) is obtained through the hydrolysis of FeCl$_3$ with boiled deionized water. The size distribution of colloids stemming from the AFM image (Figure S1a–c) indicates a relatively uniform lateral size of around 10–15 nm with a height ranging from 2–8 nm. Relying on electrostatic interaction between positively charged Fe(OH)$_3$ nanoparticles (+28 mV of zeta potential) and negatively charged polyanion (PSS, −37 mV of zeta potential), the Fe(OH)$_3$ colloids can be wrapped by PSS and form Fe(OH)$_3$@PSS clusters (−30 mV of zeta potential) through slow dropwise addition of the Fe(OH)$_3$ colloids into the PSS solution (Figure S3, S4). As expected, a larger diameter of Fe(OH)$_3$@PSS clusters than that of Fe(OH)$_3$ nanoparticles is estimated through DLS measurement, which can be attributed to the encapsulation of Fe(OH)$_3$ colloids with PSS polyanion (Figure S2, S4). After adding graphene oxide (GO) dispersion, a homogeneous GO hybrid ink

is obtained. Via a simple vacuum-assisted filtration of hybrid ink through supporters, M-1 with fusiform-like nanochannels is obtained. After etching treatment of M-1, the membrane with polyanion is retained and named M-2.

The surface morphology and cross-section information of the membranes were collected under SEM. Compared with the GOM, visible Fe(OH)$_3$@PSS clusters both exist on the surface and the cross-section of M-1, contributing to more nano-winkles (Figure S5a,b). After a post-treatment with EDTA solution, no visible Fe(OH)$_3$ nanoparticles from M-2 indicate the successful removal of Fe(OH)$_3$ nanoparticles (Figure 1b and Figure S5c). Besides, M-2 demonstrates the free-standing property (Figure 2b), which is desirable and crucial for further exploration of the membrane's ion transport behaviours. To confirm the introduction of polyanion to the GOM from the chemistry views, EDX mappings of Fe in red and S in light blue from membranes were analyzed (Figure 1e and Figure S6). The denser Fe and S element mapping signals from M-1 than that of carbon tape reveal the existence of Fe(OH)$_3$@PSS clusters inside. After etching with EDTA solution, the uniform Fe element mapping signal from M-2 and carbon tape reveals the successful removal of Fe(OH)$_3$ colloids from the membrane. In contrast, the PSS polyanion as intercalates is inside the membranes as proved by the similar S element mapping signal as M-1 when compared to that of carbon tape. ATR-FTIR is another characterization to confirm the existence of polyanion inside the membrane. As shown in Figure S7, the characteristic peaks assigned to GO containing C=O (1720 cm^{-1}), C—O (1240 cm^{-1}), C—O—C (1080 cm^{-1}) and C=C (1618 cm^{-1}) can be found both from GOM and M-2, whilst the peaks at 1153 cm^{-1}, 1124 cm^{-1}, 1030 cm^{-1} and 1006 cm^{-1} only appear in M-2, which can be attributed to the S=O stretch and SO$_2$ symmetric stretch from sulfonate groups ($-SO_3$) of PSS polyanion.[14b,17] The contact angles measurement reveals that M-1 and M-2 with similar contact angles at ~58° are more hydrophilic than the pristine GOM at ~70° (Figure S8).

Furthermore, we investigated the structure of the membranes using XRD. As is known, the d-spacing of 2D nanomaterials membranes is a vital factor for mass transport and the enlarged nanochannels have the capacity for fast ion transport. For the GOM, as shown in Figure 1c, a narrow X-ray peak with full width at a half-maximum of 0.6° can be detected at 11.3°, corresponding to the d-spacing of around 7.8 Å. After intercalation, the intense peak is displaced to a lower degree at 9.5° (d-spacing of 9.2 Å) and overlapped with newly formed peaks of 10.8° (8.2 Å) and 12.5° (7.1 Å), indicating the dis-uniform expansion of nanochannels brought by the intercalated clusters consistent with the previous study (Figure 1d).[18] Although a slight decline in d-spacing of M-2 membranes occurs after removal of the colloidal nanoparticles from nanochannels, the broad peak (full-width at half-maximum of 1.0°) still exists in comparison with GOM, indicating that the formed nano-winkles inside the membranes cannot be eliminated through the removal of nanoparticles with the post-treatment of EDTA (Figure 1d).[19] Figure 1d illustrates the nanochannels' model of the membranes. In addition, AFM confirms the formation of the fusiform-like nanochannels from another aspect (Figure 1f–h).
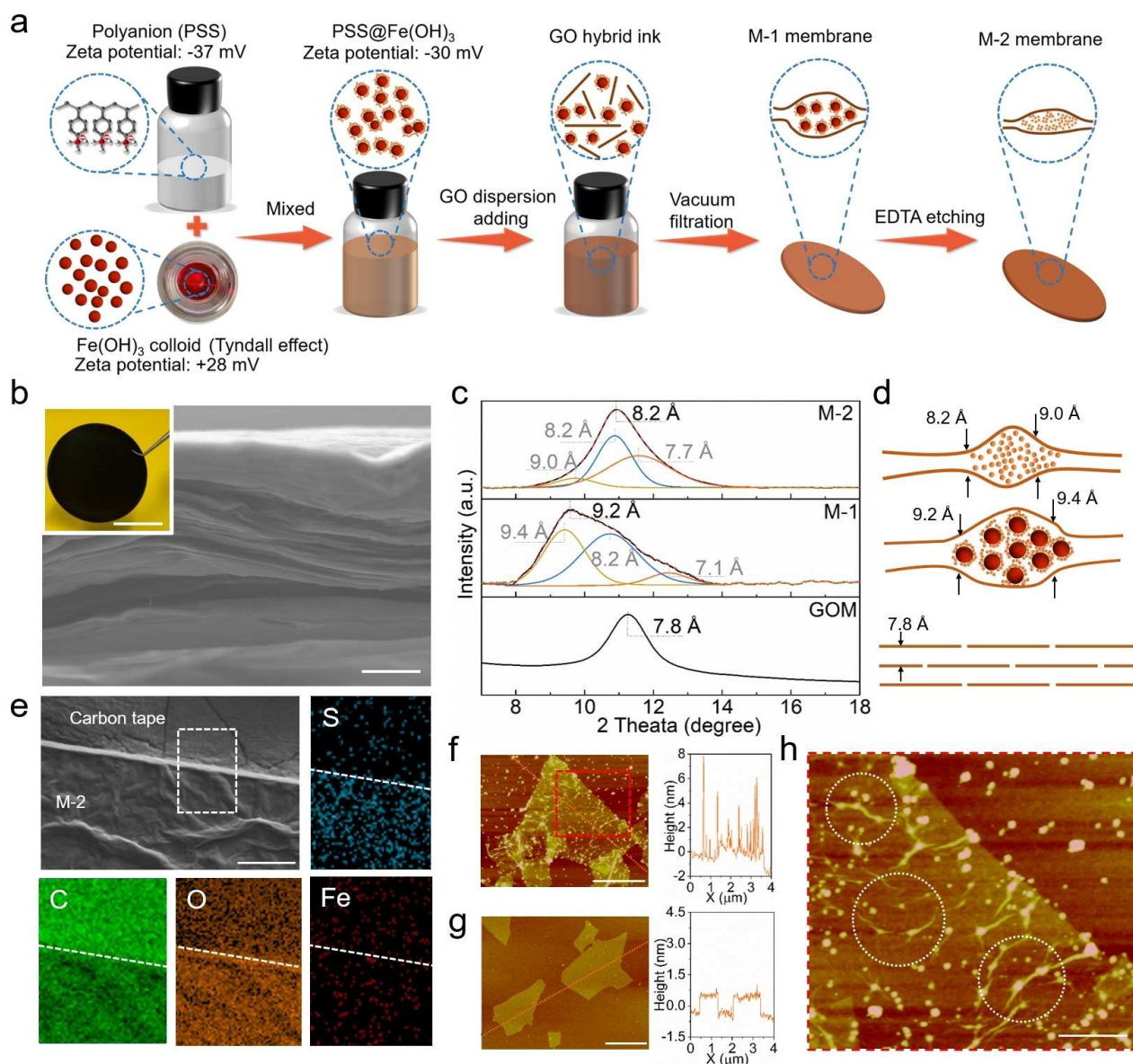
ChemSusChem

Research Article
doi.org/10.1002/cssc.202200933

Chemistry
Europe
European Chemical
Societies Publishing

Figure 1. a) Schematic illustration of the preparation of membranes. b) SEM image of M-2 and its digital photography of side view. Scale bars are 500 nm and 2 cm for SEM image and inset digital photography, respectively. c) XRD patterns of membranes in the dry state. d) Schematic illustration of the individual architecture of membranes in this study. Brown line, GO nanosheets; dark red ball, Fe(OH)$_3$ colloids; yellow ball, polyanion. e) SEM image of the M-2 membrane surface and corresponding elemental maps from the white dashed framework of (e). The scale bar is 25 μm for (e). f,g) AFM heights of GO nanosheets wrapped with and without Fe(OH)$_3$@polyanion, respectively. The scale bar is 1 μm for (f) and (g). h) The magnified image of (f) and the white short dash circles reveal the nano-winkles and fusiform-like nanochannels formed by wrapping with Fe(OH)$_3$@polyanion. The scale bar is 300 nm for (h).

The GO nanosheets with the height of 0.7–0.8 nm fully unfold on the silicon wafer without any visible nano-winkles and corrugation, contributing to the narrow nanochannels by stacking of GO nanosheets during membrane preparation. In contrast, numerous fusiform-like nanochannels with a height of ~2–8 nm formed by embedding Fe(OH)$_3$@PSS clusters inside GO nanosheets are uniformly distributed. More importantly, the initially formed nano-wrinkles can be accumulated and sustained after the etching treatment, supplying extra pathways to facilitate ion transport.

We evaluated the transmembrane ionic transport properties of the membranes by performing the ionic current-voltage (I-V)

measurements with the homemade electrochemical cell (Figures S9a–c). In Figure 2a, the measured ionic conductance through M-2 displays two distinct characteristic behaviours, which obey the linear relationship in the high concentration region and gradually reveal a plateau in the low concentration region (< 100 mM), indicating the surface-charge governed ion transportation behaviour.[20] When the KCl concentration is decreased to 10 mM, the corresponding Debye screening length is up to ~3 nm and it can fully cover the height of nanochannel inside the M-2 membrane (1.51 nm of d-spacing in the wet state) (Figure S10). Benefited from the negatively charged functionalities including —COO$^-$, —OH and —SO$_3^-$ from

ChemSusChem

Research Article
doi.org/10.1002/cssc.202200933

Chemistry
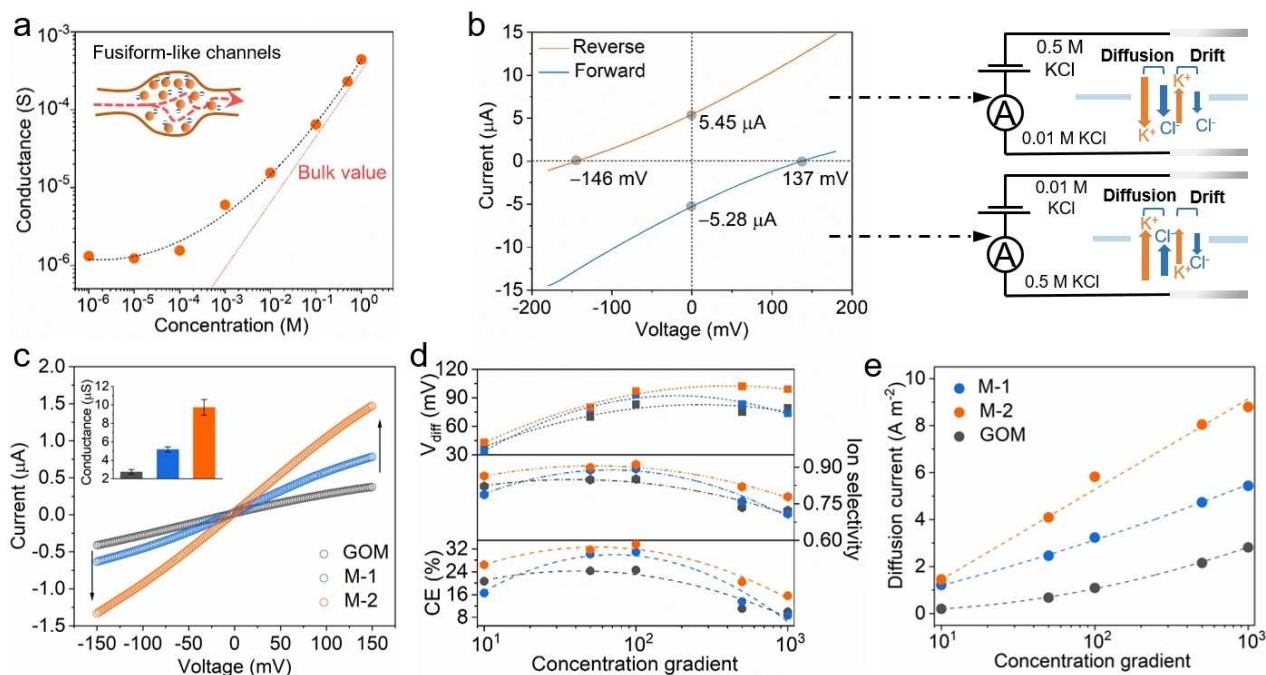**Europe**
European Chemical
Societies Publishing

Figure 2. a) Conductance for the M-2 membrane with the range of KCl concentration from 10^{-6} to 1 M. Inset: schematic illustration of fusiform-like nanochannels inside the M-2 membrane. Brown line, GO nanosheets; yellow ball, polyanions; blue ball, negative charge revealed by polyanion; red arrow: diffusion direction of cations. b) Forward and reverse diffusion I-V curves for the M-2 membrane were examined in a 50 fold KCl concentration. c) I-V responses of GOM, M-1 and M-2 with 0.01 M NaCl. Inset: the corresponding conductance of membranes. d) The V_{diff}, ion selectivity and conversion efficiency (CE) under a series of KCl concentration gradients, where the low concentration side is fixed at 10^{-5} M. Orange, M-2; blue, M-1; black, GOM. e) The diffusion current of the membranes.

the GO nanosheets and polyanion, respectively, the nanochannels from the membrane normally reveal negatively charged. Thus, cations will enrich the nanochannel and anions with the negative charge will be repulsed, forming a confined unipolar environment. The conductance of membranes calculated from the slope of the ionic current-voltage (I-V) curves at the 10 mM NaCl aqueous solution reflects the mass transport behaviours of the corresponding membranes. As shown in Figure 2c, M-2 reveals the highest conductance of 10 μS in 10 mM NaCl, which is nearly 2 fold and 4 fold higher than that of M-1 and GOM membranes, respectively. Obviously, the improved mass transport performance of M-2 can be ascribed to the enlarged d-spacing of the nanochannels when compared to that of the pristine GOM (Figure 1c and Figure S10). A similar phenomenon has been also observed in previous studies, where the enlarged nanochannels of the two-dimensional membranes can accelerate the water or ion transport across the membrane for specific purposes.[21] Besides, it is worth noting that the difference in conductance of M-1 and M-2 can be attributed to the steric hindrance effect of $Fe(OH)_3$ colloidal nanoparticles, impeding the mass transport of M-1. To demonstrate it, we then examined the effect of temperature on ion transportation of membranes by using I-V measurement. Based on the Arrhenius equation, the energy barriers for Na^+ passage towards the membrane can be easily calculated, following the order of M-2 < M-1 < GOM (Figure S11). The lower the energy barrier is, the easier it is for Na^+ to penetrate the membrane.[22]

Based on the moderate d-spacing of nanochannels in M-2, the optimized ion transportation behaviour can be attributed to the alleviated steric hindrance effect of the intercalating agents.

When the negatively charged membrane is under the salinity concertation gradient system, the directional cation flow across the membrane along the concentration gradient direction can induce the net diffusion current (I_{diff}) and potential (V_{diff}), which further provides us with an insight into the confined ion transport process.[21a,23] The cation-selective performance of M-2 under a salinity gradient was studied by choosing different concentrations of KCl electrolytes filled at the membrane sides. Figure 2b shows the representative I-V curves of M-2 under a 50 fold concentration gradient (0.5 M/ 0.01 M KCl). The open-circuit potential (V_{ocp}) and short-circuit current (I_{sc}) are 137 mV and 5.28 μA in the forward direction, respectively. Under a reverse gradient concentration, the values of V_{ocp} and I_{sc} at 146 mV and 5.45 μA are collected from the intercepts on the X/Y-axes. The similar value of V_{ocp}, as well as I_{sc}, under the forward and reverse direction, indicates the symmetric membrane structure with neglectable ion rectification phenomenon. Next, the cation selectivity and CE of the membranes were further explored under a series of concentration gradients (Figures 2d,e). Obviously, M-2 reveals the highest I_{diff} and V_{diff} when compared to the others, indicating the enhanced ion transport behaviour synthetically caused by the enlarged nanochannels and increased space charge from polyanion. Although the V_{diff} of each membrane gradually

ChemSusChem

Research Article
doi.org/10.1002/cssc.202200933

Chemistry
Europe
European Chemical
Societies Publishing

increases as the concentration gradient raises, a slight voltage drop in membranes is observed under a high concentration gradient, which is likely due to the relatively strong ion concentration polarization (ICP) effect at the surface of the membrane.[14] By subtracting V_{redox} from V_{ocp} (Supporting Information 1 and Table S1), the cation selectivity quantified as cation transference numbers of M-2 membrane can exceed 0.9 with 32% energy conversion efficiency, displaying the comparable performance with that of other 2D-based membranes on osmotic energy harvest.[20,21,24]

In order to replicate the concentration gradient energy harvest system realistically, the same volume of 0.01 and 0.5 M NaCl electrolyte solutions simulated as river water and seawater were separated with the membrane in the electrochemical cell (Figure S9a). The ionic current-voltage (*I-V*) measurements were applied to determine the values of V_{ocp} and I_{sc} of each membrane. GOM maintain a high V_{ocp} of ~129 mV but reveal a low I_{sc} of ~1.7 μA (Figure 3a). This can be attributed to the compressed nanochannels induced high cation selectivity and restricted cation flux across the membrane (Figure 3d). Along with the introduction of $Fe(OH)_3$@polyanion inside the membrane, the *d*-spacing of nanochannels of M-1 is expanded to 16.1 Å in the wet state (Figure S10), which is beneficial for the fast cation transport and high transmembrane flux. As a result, the corresponding I_{sc} is improved to ~3.7 μA with a low value of V_{ocp} at ~119 mV, which could be ascribed to the synergetic
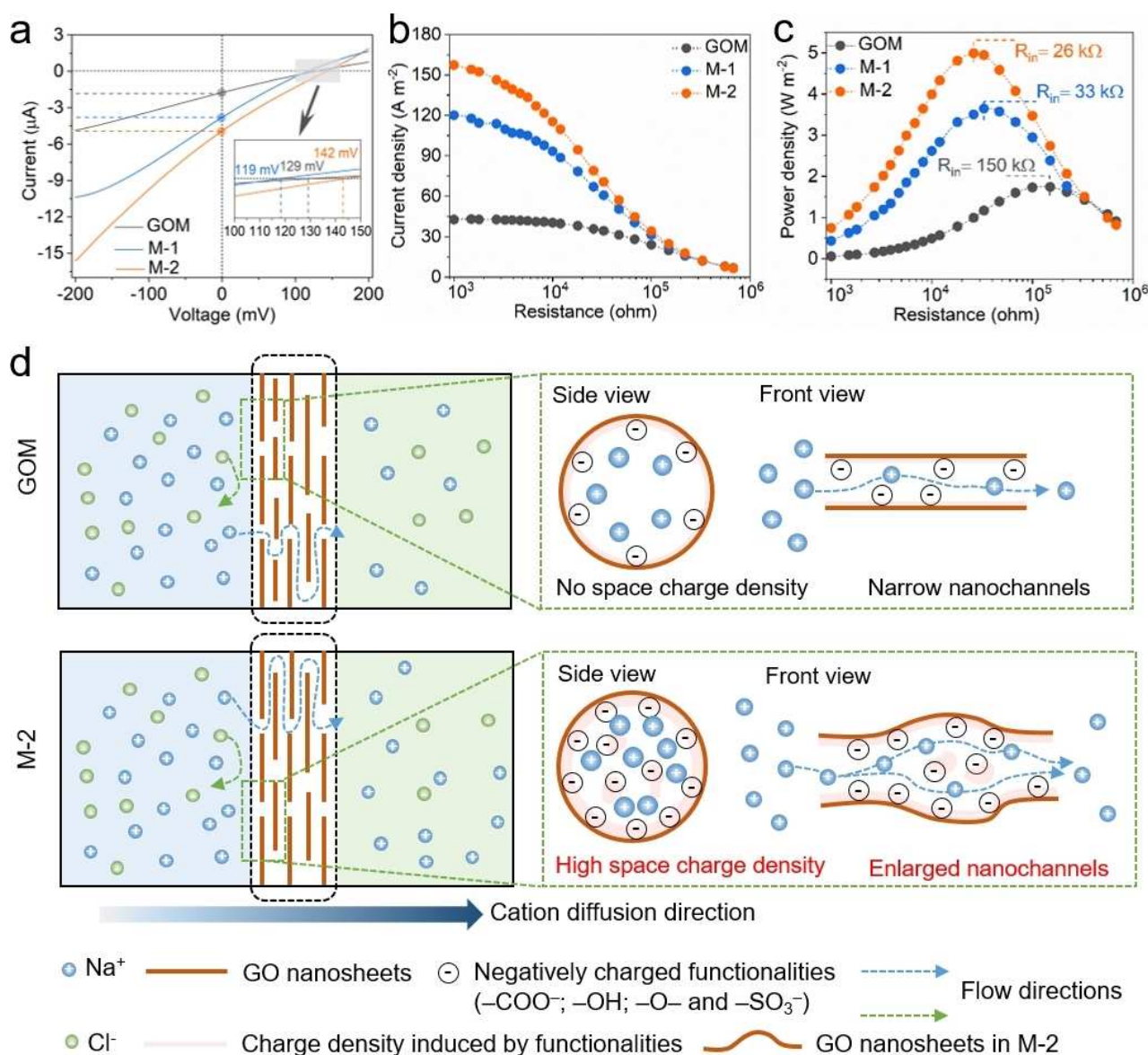

Figure 3. a) I–V curves for M-2 versus GOM and M-1, revealing enhanced ion transport with high cation selectivity. b,c) Current density and power density of the M-2 membrane as functions of an electronic load resistor under 50-fold NaCl concentration. d) Schematic diagram of ion transport behaviours of GOM and M-2 membrane. For GOM, narrow nanochannels with no space charge density inside the nanochannels result in limited cation transport with high cation selectivity, revealing low I_{sc} with high V_{ocp}. For M-2 membrane, the fusiform-like nanochannels embedded with polyanion indicate the large nanochannel height with high surface and space charge density, contributing to high I_{sc} and V_{ocp}.

effect of spacing charge, surface charge and interlayer distance. Besides, the direct introduction of $Fe(OH)_3$ colloidal nanoparticles to GOM can improve the flux of ion transport, but is detrimental to cation selectivity, because the negative charge from GO nanosheets can be partially neutralized with positively charged colloidal nanoparticles (Figure S13). Intriguingly, after etching treatment, the value of V_{ocp} and I_{sc} of M-2 simultaneously boosts to ~ 142 mV and ~ 4.9 μA, respectively. As the ion transport mechanism proposed in Figure 3d and Figure S12, the enhanced cation selectivity together with the fast cation flux across the membrane can be ascribed to two reasons. Firstly, the blocked nanochannels inside the membrane are re-opened to reduce the ion transport barriers and allow fast cation transport after the removal of colloidal nanoparticles. Secondly, the space charge from $-SO_3$ of PSS partially neutralized by $Fe(OH)_3$ nanoparticles are reactivated to realize the high cation selectivity by removing the encapsulated positively charged nanoparticles. As reflected by the zeta potential measurements, the more negatively charged polyanion compared to GO dispersion not only provides space charge to the enlarged nanochannels but also enhances the membrane surface charge density (Figure S3 and Figure S14). Consequently, on the basis of the V_{ocp} and I_{sc}, the maximum power density (P_{max}) of each membrane can be estimated as in Equation (1).

$$P_{max} = V_{ocp} \times I_{sc}/(4 \times A_{membrane\ area}) \qquad (1)$$

Apparently, M-2 exhibits the highest theoretical power density of around 5.80 W m^{-2}, yielding about 1.6 fold and 3.5 fold maximum power output density than that of M-1 and GOM membranes, respectively.

In order to extract electricity from this system, a series of external resistances as the external circuit was supplied. As the loading resistance raises gradually, the current density of the external circuit for each membrane declines accordingly (Figure 3c). When the loading resistance is equal to the internal resistance of the membrane, the maximum practical output power density, calculated as depicted in Equation (2), is achieved.

$$P_{output} = I^2 \times R_L \qquad (2)$$

As shown in Figure 3c, compared with pristine and M-1, M-2 performs the highest output power density of ~ 4.94 W m^{-2} with the lowest internal resistance of 26 kΩ, which can be attributed to the synergetic effect of the enlarged nanochannels and the high space charge density (Figure 3d).

We found that the nanochannel density of M-2 is crucial for power density (Figure S15 and Table S2). When the loading of pore makers is low, underdeveloped nanochannels fail to provide sufficient pathways for ion transportation, limiting power density. In contrast, for the relatively high loading, numerous nanochannels intended to improve the power output can induce the inevitable ICP phenomenon near the membrane surface or affect the membrane integrity during the electro-chemical tests, deteriorating the ion transportation and restrict-

ing the power density.[25] Besides, the thickness exerts a substantial impact on the power density as well (Figures S16a,b). When the thickness is decreased to around 2.9 μm, M-2 with poor mechanical integrity undergoes the de-laminating phenomena during the electrochemical tests. In contrast, poor ion transportation occurs when passing through the relatively thick membrane, increasing the ion resistance and slightly decreasing the performance of power density.[12b] Meanwhile, directly introducing polyanion to GOM can endow the membrane with a high V_{ocp} of 139 mV but a restricted I_{sc} of 4.1 μA, causing a low power density of around 4.7 W m^{-2} in comparison with M-2 (Figure S17b). This distinct difference in ion flux (I_{sc}) reflects the loose structure of M-2 that enables to facilitate the fast ion permeability, whilst the direct combination of polyelectrolytes with GO cannot form numerous nano-wrinkles or provide extra pathways for efficient cation passage (Figures S17a and 1 h).

More importantly, M-2 can sustain the stable and high-performance power density of around 5.5 W m^{-2} with the negligible fluctuation in I_{sc} and V_{ocp} for 14 days under a 50 fold NaCl gradient, indicating its chemical stability and mechanical integrity even after a long-term exposure under an osmotic environment (Figures 4a,b).

For practical applications, various working conditions were considered to evaluate the performance of M-2. When the membrane testing area was decreased from 19.625 to 0.03 mm^{-2}, the corresponding power density rapidly increased from 0.06 to 5.8 W m^{-2} (Figure S18). Besides, we find that the performance of M-2 highly depends on the pH value of the solution as the osmotic energy conversion is mainly influenced by the surface charge of GO nanosheets and the space charge of polyanion. In the acidic environment, the protonation process of $-COO^-$ and $-SO_3^-$ from the membrane can restrict the surface charge and space charge, which leads to a poor power density of ~ 3.6 W m^{-2}. When the pH value of the electrolyte raises, the deprotonation of functional groups enhances the charge density of the membrane, improving the performance up to ~ 5.6 W m^{-2} under the alkali environment (Figure 4c). Apart from seawater, various kinds of water resources from natural and human activities considered as the replaceable high concentration side were selected to examine the osmotic energy harvest performance of M-2 (Figure 4d and Figures S19a–d). Then the draw solution was fixed with artificial river water (0.01 M NaCl), artificial water resources with different salinity as feed solution can induce different concentration gradients of 21 fold, 128 fold, 300 fold and 428 fold, respectively, facilitating the membrane to obtain the power density of 2.2, 6.6, 12.8 and 14.7 W m^{-2}, respectively. Furthermore, various types of electrolytes including HCl, KCl, NaCl, $CaCl_2$ and $FeCl_3$, respectively, as osmotic power sources are also selected to study the energy conversion behaviour of the membrane (Figure 4e). Although the same 50 fold concentration gradients of electrolytes are applied to the system, the obtained power density of the membrane from diverse electrolytes is dramatically different. In particular, the maximum power output achieved from HCl is up to 34.1 W m^{-2}, which is nearly 3.7 fold and 5.8 fold higher than that of KCl and NaCl electrolytes,

ChemSusChem

Research Article
doi.org/10.1002/cssc.202200933

Chemistry
Europe

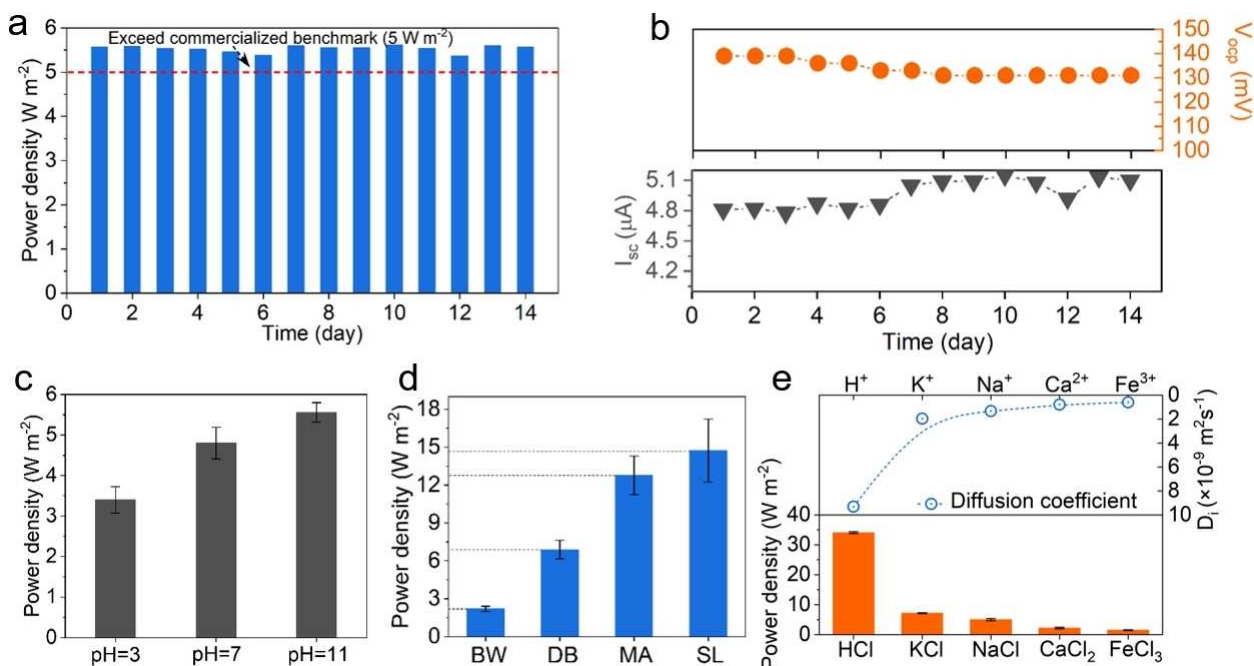European Chemical
Societies Publishing

Figure 4. a) A long-term operation test of M-2 without electrolyte replenished under artificial seawater and river water system. b) Corresponding fluctuation in V_{ocp} and I_{sc} of M-2. c) Influence of the pH of the electrolyte solution on the power density of M-2. d) Power generation of M-2 under a series of artificial water resources including brackish water (BW), desalination brines (DB), brines from mining activities (MA), and water from the salt lake (SL). e) Power generation of M-2 membrane under a series of chloride salts with different cation valence.

respectively. The huge difference in power output between HCl and other monovalent cation electrolytes can be ascribed to two reasons. Firstly, compared with other monovalent cations (K^+ and Na^+), the high value of the cation diffusion coefficient for H^+ (9.31×10^{-9} $m^2 s^{-1}$) represents the fast cation diffusion transport across the cation-selective membrane, which facilitates the efficient charge separation process and contributes to the outstanding power output from HCl electrolyte.[26] Secondly, the order for the hydrated radii of ions is Na^+ (0.36 nm) > K^+ (0.33 nm) > H^+ (0.28 nm). The smaller the hydrated radius of the ion is, the lower the transport barrier occurs when penetrating through the membrane. For multivalent cation electrolytes, this system reveals poor power output of below 2.5 $W m^{-2}$. Apart from the low cation diffusion coefficient and large hydrated radii of Ca^{2+} and Fe^{3+}, the negative influence such as chelation, electrostatic loading and uphill transport between multivalent cations and the membrane can also worsen the power output from multivalent cation electrolytes.[16,27] Thus, water sources such as seawater and acid wastewater, which contain enormous monovalent cation, are more potentially suitable as the sources of osmotic power generation than multivalent cation electrolytes.

Conclusion

In this study, one kind of 2D lamellar membrane with highly charged fusiform-like nanochannels for high-performance osmotic energy conversion was developed. The encapsulated

colloids@polyanion clusters inside the membrane played important roles not only to expand the nanochannels as the space holder but also to provide extra space charge on osmotic energy harvest followed by the EDTA dissolution of colloidal nanoparticles. Compared with pristine GOM, M-2 demonstrated a high cation selectivity over 0.9 with an energy conversion efficiency of up to 32%. Besides, it revealed the maximum power output of ~4.94 $W m^{-2}$ under a 50 fold electrolyte gradient with the combination of enlarged nanochannels and enhanced space charge. The power density could be easily boosted up to 14.7 and 37.4 $W m^{-2}$ by selecting the saline water and HCl electrolyte respectively as the osmotic power generation sources. Overall, our work not only revealed that M-2 with the enhanced cation transport property has potential practical application in osmotic energy conversion, but also provided a material design strategy to improve ion transport for the development of other membrane-based osmotic energy conversions.

Experimental Section

Preparation of Fe(OH)₃ colloids

2.5 g $FeCl_3$ was dissolved into 4 mL deionized water to get $FeCl_3$ solution. Next, 0.1 mL of the solution was very slowly dropped into 100 mL of boiling deionized water. $Fe(OH)_3$ colloids were obtained after the water was kept boiling for 2 minutes.[28]

Preparation of GOM, M-1 and M-2 membranes

The freestanding GOMs with a thickness of ~2 μm were prepared via vacuum-assisted filtering GO dispersion on the AAO membrane.

For fabrication of free-standing M-1: typically, the diluted $Fe(OH)_3$ dispersion was slowly added to 100 mL PSS solution (0.1 mg/mL) under a magnetic stirring at room temperature followed by a 60 min sonication. Next, GO dispersion was slowly dropped to the mixed solution and kept the vigorous stirring for another 60 min. Finally, the obtained solution was filtered through the supporter.

For obtaining free-standing M-2: M-1 firstly experienced a mild thermal annealing procedure (80 °C for overnight) to maintain the aqueous stability, then the membrane was immersed in 0.1 M EDTA solution to remove the embedded colloidal nanoparticles followed by washing with DI water repeatedly. Then the membrane was kept at room temperature under a vacuum oven. In order to improve the aqueous stability of membranes during the electrochemical tests, a mild thermal annealing procedure (80 °C for overnight) was applied to M-1 before further usage.[20,29]

Conflict of Interest

The authors declare no conflict of interest.

Data Availability Statement

The data that support the findings of this study are available from the corresponding author upon reasonable request.

[1] Z. W. Seh, Y. Sun, Q. Zhang, Y. Cui, *Chem. Soc. Rev.* **2016**, *45*, 5605–5634.

[2] a) B. E. Logan, M. Elimelech, *Nature* **2012**, *488*, 313–319; b) F. La Mantia, M. Pasta, H. D. Deshazer, B. E. Logan, Y. Cui, *Nano Lett.* **2011**, *11*, 1810–1813.

[3] a) N. Y. Yip, M. Elimelech, *Environ. Sci. Technol.* **2012**, *46*, 5230–5239; b) N. Y. Yip, D. A. Vermaas, K. Nijmeijer, M. Elimelech, *Environ. Sci. Technol.* **2014**, *48*, 4925–4936.

[4] R. Pattle, *Nature* **1954**, *4431*, 1.

[5] J. Feng, M. Graf, K. Liu, D. Ovchinnikov, D. Dumcenco, M. Heiranian, V. Nandigana, N. R. Aluru, A. Kis, A. Radenovic, *Nature* **2016**, *536*, 197–200.

[6] a) L.-H. Y. Yi-Cheng Liu, Min-Jie Zheng, Kevin C.-W. Wu, *Sci. Adv.* **2020**, *7*, 9924; b) X. Zhao, C. Lu, L. Yang, W. Chen, W. Xin, X.-Y. Kong, Q. Fu, L. Wen, G. Qiao, L. Jiang, *Nano Energy* **2021**, *81*, 105657.

[7] a) Z. Wang, Z. Zhang, H. Qi, A. Ortega-Guerrero, L. Wang, K. Xu, M. Wang, S. Park, F. Hennersdorf, A. Dianat, A. Croy, H. Komber, G. Cuniberti, J. J. Weigand, U. Kaiser, R. Dong, X. Feng, *Nature Synthesis* **2021**, *1*, 69–76; b) X. Zuo, C. Zhu, W. Xian, Q. W. Meng, Q. Guo, X. Zhu, S. Wang, Y. Wang, S. Ma, Q. Sun, *Angew. Chem. Int. Ed. Engl.* **2022**, *61*,

e202116910; c) W. Xian, X. Zuo, C. Zhu, Q. Guo, Q. W. Meng, X. Zhu, S. Wang, S. Ma, Q. Sun, *Nat. Commun.* **2022**, *13*, 3386.

[8] X. Liu, M. He, D. Calvani, H. Qi, K. Gupta, H. J. M. de Groot, G. J. A. Sevink, F. Buda, U. Kaiser, G. F. Schneider, *Nat. Nanotechnol.* **2020**, *15*, 307–312.

[9] a) P. Liu, T. Zhou, L. Yang, C. Zhu, Y. Teng, X.-Y. Kong, L. Wen, *Energy Environ. Sci.* **2021**, *14*, 4400–4409; b) X. Lin, P. Liu, W. Xin, Y. Teng, J. Chen, Y. Wu, Y. Zhao, X. Y. Kong, L. Jiang, L. Wen, *Adv. Funct. Mater.* **2021**, *31*, 2105013.

[10] a) S. Qin, D. Liu, G. Wang, D. Portehault, C. J. Garvey, Y. Gogotsi, W. Lei, Y. Chen, *J. Am. Chem. Soc.* **2017**, *139*, 6314–6320; b) J. J. Shao, K. Raidongia, A. R. Koltonow, J. Huang, *Nat. Commun.* **2015**, *6*, 7602; c) J. Lao, R. Lv, J. Gao, A. Wang, J. Wu, J. Luo, *ACS Nano* **2018**, *12*, 12464–12471.

[11] a) H. Huang, Z. Song, N. Wei, L. Shi, Y. Mao, Y. Ying, L. Sun, Z. Xu, X. Peng, *Nat. Commun.* **2013**, *4*, 2979; b) Y. Y. Luwei Sun, H. Huang, Z. Song, Y. Mao, Z. Xu, X. Peng, *ACS Nano* **2014**, *8*; c) L. Ding, Y. Wei, Y. Wang, H. Chen, J. Caro, H. Wang, *Angew. Chem. Int. Ed. Engl.* **2017**, *56*, 1825–1829; d) D. Xu, X. Zhu, X. Luo, Y. Guo, Y. Liu, L. Yang, X. Tang, G. Li, H. Liang, *Environ. Sci. Technol.* **2021**, *55*, 1270–1278.

[12] a) W. Xin, L. Jiang, L. Wen, *Acc. Chem. Res.* **2021**, *54*, 4154–4165; b) Z. Zhang, L. Wen, L. Jiang, *Nat. Rev. Mater.* **2021**, *6*, 622–639.

[13] Y. Wu, T. Zhou, Y. Wang, Y. Qian, W. Chen, C. Zhu, B. Niu, X.-Y. Kong, Y. Zhao, X. Lin, L. Jiang, L. Wen, *Nano Energy* **2022**, *92*.

[14] a) Y. Y. Yi Guo, Y. Mao, X. Peng, B. Chen, *Angew. Chem. Int. Ed.* **2016**, *55*; b) M. Zhang, K. Guan, Y. Ji, G. Liu, W. Jin, N. Xu, *Nat. Commun.* **2019**, *10*, 1253.

[15] Z. Lu, Y. Wu, L. Ding, Y. Wei, H. Wang, *Angew. Chem. Int. Ed. Engl.* **2021**, *60*, 22265–22269.

[16] Z. Zhang, L. He, C. Zhu, Y. Qian, L. Wen, L. Jiang, *Nat. Commun.* **2020**, *11*, 875.

[17] Y. Qian, J. Shang, D. Liu, G. Yang, X. Wang, C. Chen, L. Kou, W. Lei, *J. Am. Chem. Soc.* **2021**, *143*, 5080–5090.

[18] a) Q. Yang, Y. Su, C. Chi, C. T. Cherian, K. Huang, V. G. Kravets, F. C. Wang, J. C. Zhang, A. Pratt, A. N. Grigorenko, F. Guinea, A. K. Geim, R. R. Nair, *Nat. Mater.* **2017**, *16*, 1198–1202; b) W. L. Xu, C. Fang, F. Zhou, Z. Song, Q. Liu, R. Qiao, M. Yu, *Nano Lett.* **2017**, *17*, 2928–2933.

[19] D. V. Andreeva, M. Trushin, A. Nikitina, M. C. F. Costa, P. V. Cherepanov, M. Holwill, S. Chen, K. Yang, S. W. Chee, U. Mirsaidov, A. H. Castro Neto, K. S. Novoselov, *Nat. Nanotechnol.* **2021**, *16*, 174–180.

[20] W. Xin, H. Xiao, X. Y. Kong, J. Chen, L. Yang, B. Niu, Y. Qian, Y. Teng, L. Jiang, L. Wen, *ACS Nano* **2020**, *14*, 9701–9710.

[21] a) Z. Zhang, S. Yang, P. Zhang, J. Zhang, G. Chen, X. Feng, *Nat. Commun.* **2019**, *10*, 2920; b) J. Wang, Z. Zhang, J. Zhu, M. Tian, S. Zheng, F. Wang, X. Wang, L. Wang, *Nat. Commun.* **2020**, *11*, 3540.

[22] a) Z. Lu, Y. Wei, J. Deng, L. Ding, Z. K. Li, H. Wang, *ACS Nano* **2019**, *13*, 10535–10544; b) J. Abraham, K. S. Vasu, C. D. Williams, K. Gopinadhan, Y. Su, C. T. Cherian, J. Dix, E. Prestat, S. J. Haigh, I. V. Grigorieva, P. Carbone, A. K. Geim, R. R. Nair, *Nat. Nanotechnol.* **2017**, *12*, 546–550.

[23] N. Sheng, S. Chen, M. Zhang, Z. Wu, Q. Liang, P. Ji, H. Wang, *ACS Appl. Mater. Interfaces* **2021**, *13*, 22416–22425.

[24] a) Y. Wu, W. Xin, X.-Y. Kong, J. Chen, Y. Qian, Y. Sun, X. Zhao, W. Chen, L. Jiang, L. Wen, *Mater. Horiz.* **2020**, *7*, 2702–2709; b) G. Yang, D. Liu, C. Chen, Y. Qian, Y. Su, S. Qin, L. Zhang, X. Wang, L. Sun, W. Lei, *ACS Nano* **2021**, *15*, 6594–6603.

[25] J. Gao, X. Liu, Y. Jiang, L. Ding, L. Jiang, W. Guo, *Small* **2019**, *15*, e1804279.

[26] a) C. Chen, G. Yang, D. Liu, X. Wang, N. A. Kotov, W. Lei, *Adv. Funct. Mater.* **2021**, *32*; b) W. Sparreboom, A. van den Berg, J. C. Eijkel, *Nat. Nanotechnol.* **2009**, *4*, 713–720.

[27] a) P. Sun, R. Ma, H. Deng, Z. Song, Z. Zhen, K. Wang, T. Sasaki, Z. Xu, H. Zhu, *Chem. Sci.* **2016**, *7*, 6988–6994; b) M. Z. Pengzhan Sun, K. Wang, M. Zhong, J. Wei, D. Wu, Z. Xu, H. Zhu, *ACS Nano* **2013**, *7*; c) P. Sun, K. Wang, J. Wei, M. Zhong, D. Wu, H. Zhu, *J. Mater. Chem. A* **2014**, *2*, 7734–7737.

[28] M. Du, C. Xu, J. Sun, L. Gao, *J. Mater. Chem. A* **2013**, *1*, 7154–7158.

[29] J. Ji, Q. Kang, Y. Zhou, Y. Feng, X. Chen, J. Yuan, W. Guo, Y. Wei, L. Jiang, *Adv. Funct. Mater.* **2017**, *27*, 1603623.